Supplementary information for

Deep evolution of carbonated magmas controls ocean island basalt chemistry

Junlong Yang[1], Chao Wang[2,*], Zhenmin Jin[2], Zhicheng Jing[1,*]

[1]Department of Earth and Space Sciences, Southern University of Science and Technology, Shenzhen, 518055, China

[2]State Key Laboratory of Geological Processes and Mineral Resources, School of Earth Sciences, China University of Geosciences, Wuhan, 430074, China

[*]Corresponding to: jingzc@sustech.edu.cn; wangchao@cug.edu.cn

Contents of this file

Supplementary Text 1: Justification of the selected picritic melt composition as the primary magma composition

Here we consider the picritic melt is extracted from the source peridotite in the upper mantle and accumulated at the base of lithosphere for high-pressure crystallization. Thus, the crystallization experiments were conducted at 3 GPa, corresponding to the pressure at the base of a typical oceanic lithosphere with a thickness of ~100 km (ref. [1]). Partial melting of peridotite likely occurs at a pressure higher than the crystallization pressure and the composition of the primary magma partially depends on the melting pressure. However, the difference in pressures is likely small because the degree of melting increases with decreasing depth. As a result, most melts would be produced at shallow depths right before crystallization. We therefore selected the picritic melt composition based on partial melting experiments of carbonated peridotite conducted at 3 GPa, matching the pressure of our high-pressure crystallization experiments. This pressure condition was also used in ref. [2] for studying the generation of primary OIB magmas. In addition, using the same pressures for melting and high-pressure crystallization processes represents an endmember condition that can facilitate comparison of the melt compositions between the two processes.

The melting temperature of ~1450 °C for the carbonated peridotite source was determined based on the following arguments: On the one hand, the potential temperatures (T_p) of most alkalic OIBs are lower than that of Hawaiian lavas (T_p=1600 °C), whose primary magmas are estimated to have ~19 wt% MgO (ref. [3]). Therefore, the primary magmas of most alkalic OIBs should have MgO contents less than ~19 wt%. According to ref. [2], the partial melting of carbonated peridotite with 1wt.% CO_2 can produce melts with MgO contents less than ~19 wt% at temperatures lower than 1500 °C. On the other hand,

the lowest T_p of alkalic OIBs is ~1350 °C, suggesting a mantle temperature higher than 1400 °C at 3 GPa beneath most ocean islands (Fig. 4d). Therefore, we selected the picritic melt composition formed at a temperature of ~1450 °C (ref. [2]). In fact, the variations in melt compositions observed by ref. [2] in the temperature ranges of 1400-1500 °C are sufficiently small and therefore small changes in melting temperatures would not affect our conclusions.

Supplementary Text 2: Evolution of major oxide components other than MgO, FeO, and SiO_2

As demonstrated in Supplementary Fig. 6, both Al_2O_3 and Na_2O contents of melts derived from our high-pressure crystallization experiments can match that of natural alkalic OIBs at similar MgO contents (~16-18 wt%). The subsequent reactions between the HP-derived melts and the lithosphere would further increase Al_2O_3 and Na_2O contents while decreasing MgO contents as shown by the blue trend lines in Supplementary Figs. 9a-b. Thus, the OIB Al_2O_3 and Na_2O contents can be fully reproduced by our model.

Both CaO and TiO_2 show some discrepancies between our experimental results and the natural OIB compositions, likely due to the effects of source compositions. The CaO contents in our HP-derived melts are somewhat higher than those of natural alkalic OIBs, likely caused by their higher sensitivity to source CO_2 content than other major components. As shown in Supplementary Fig. 6c, the CaO content in the primary melt depends strongly on the CO_2 content of the source peridotite (grey lines), in contrast to the behaviors of other components. If the source peridotite had a CO_2 content lower than 1 wt%, the CaO contents in the HP-derived melts would fall in the range of 10-18 wt% (see below for calculation

details) and hence the OIB CaO contents can be reproduced. In fact, the estimated CO_2 contents in the source peridotite from our model are around 0.4 wt% for most alkalic OIBs, also consistent with estimates from previous study[4]. The TiO_2 contents of HP-derived melts are lower than those of natural alkalic OIBs (Supplementary Fig. 6d), suggesting that some extra TiO_2 contribution from source materials such as contamination of subducted components, as discussed in ref. [5], is required to explain the OIB TiO_2 contents.

The effects of source compositions on CaO and TiO_2 can be quantitatively evaluated using the bulk partition coefficients for Ca and Ti determined from our high-pressure crystallization experiments (Supplementary Fig. 5b and 5e). Considering mass balance during equilibrium crystallization, the normalized CaO or TiO_2 content (i.e., normalized on the CO_2-free basis) in the HP-derived melt can be expressed as:

$$\bar{X}_j^{HP-derived} = \frac{\bar{X}_j^0}{D_j(1-MF)+MF}, \quad \text{(S1)}$$

where $\bar{X}_j^0$ and $\bar{X}_j^{HP-derived}$ represent the oxide contents of element *j* (*j*=Ca or Ti) in the primary melt and the melts derived from high-pressure crystallization, respectively. D_j is the bulk solid-melt partition coefficient of element *j*; MF is the melt fraction during high-pressure crystallization. Using Eq. (S1), the CaO and TiO_2 contents in HP-derived melts can be calculated for any given CaO and TiO_2 contents in the primary melts. With 10-12 wt% CaO and 1.6-2.0 wt% TiO_2 in primary magmas, corresponding to <1 wt% CO_2 and <10% of subducted materials, respectively, the resulted CaO and TiO_2 contents of melt derived from high-pressure crystallization can match those observed in natural alkalic OIBs (Supplementary Fig. 6c and 6d).

Supplementary Text 3: Effects of adding subducted materials to the composition of

source peridotite

The TiO_2 contents in natural alkalic OIBs are roughly 30-50% higher than that of HP-derived melts from our experiments, when compared at similar MgO contents (~16-18 wt%) (Supplementary Fig. 6d). Thus, an increase of TiO_2 content by 30-50% in the mantle source by adding subducted materials would be sufficient to explain the discrepancies in TiO_2 contents. The addition of a small amount of subducted materials (e.g. GLOSS[6], MORB[7], or AOC[8]) can considerably increase the TiO_2 content of the source peridotite but has limited influences on other major elements. Here we calculated the compositions of contaminated source peridotite by mixing 5 wt% potential subducted materials including GLOSS, MORB, or AOC and presented the calculation results in Supplementary Table 6. As seen in the table, the changes in the concentrations of major components are mostly less than 10% (SiO_2: 1-2%; Al_2O_3: 11-18%; FeO^T: 1-3%; MgO: 4-5%; CaO: 3-9%), but is about 20-80% for TiO_2 due to its enrichment in the subducted materials. This means the corresponding changes in the HP-derived melts would be relatively small for most major components except for TiO_2. For Na_2O and K_2O, they are likely depleted in subducted materials because these components would likely dissolve into aqueous fluids or hydrous melts released during dehydration of subducting slabs and be transported to the mantle wedge[9]. Thus, the influence of subducted material on the alkali contents of source peridotite for OIBs would be small.

Supplementary Text 4: Correlation between the crystallization fraction and potential temperature

In Supplementary Fig. 10, we plot the calculated crystallization fraction of OIBs

against mantle potential temperature (T_P) and lithospheric thickness for various ocean islands. The lithospheric thickness, defined as the depth of the lithosphere-asthenosphere boundary (LAB) during ocean island volcanism, for each individual ocean island is provided in ref. [1]. For global alkalic OIBs, the crystallization fraction shows weak correlations with both potential temperature (r^2=0.19) and lithospheric thickness (r^2=0.17). However, when considering alkalic OIB data with LAB depths greater than ~66 km, where high-pressure crystallization is effective, the correlation between crystallization fraction and T_p becomes stronger with a r^2 of 0.39, while the correlation with the lithospheric thickness remains weak (r^2=0.15). This suggests that a correlation between crystallization fraction and T_p likely exists for ocean islands with lithospheric thickness greater than ~66 km.

Supplementary Text 5: Thermal gradient calibration experiments

The thermal gradient calibration method[10] based on the growth rate of spinel ($MgAl_2O_4$) at the interface between MgO and Al_2O_3 was used to estimate the thermal gradients across the samples (Supplementary Fig. 11) in both multi-anvil and piston-cylinder presses. Calibration experiments were conducted at pressures of 3.0 GPa and 1.0 GPa, respectively, and at temperature of 1400 °C for 4 hours. The cross-sections of the run products for the calibration experiments were examined using a SEM in the backscattered electron (BSE) mode. The temperature variations in the samples were calculated from the measured thicknesses of the spinel layer[10]. The results indicate that the spinel layer thickness remains nearly constant across the sample (Supplementary Fig. 11), suggesting a temperature gradient of less than 25 °C in samples of both experiments.

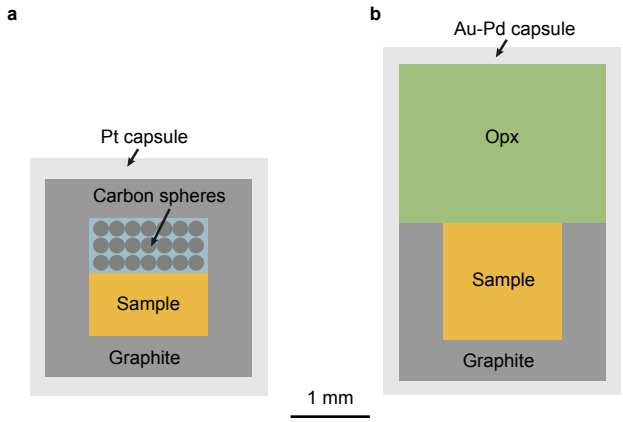

Supplementary Fig. 1. Sample configurations and capsulation. a, Sample capsule used in the multi-anvil press for high-pressure crystallization experiments. **b**, Sample capsule used in piston-cylinder press for melt-orthopyroxene reaction experiments.

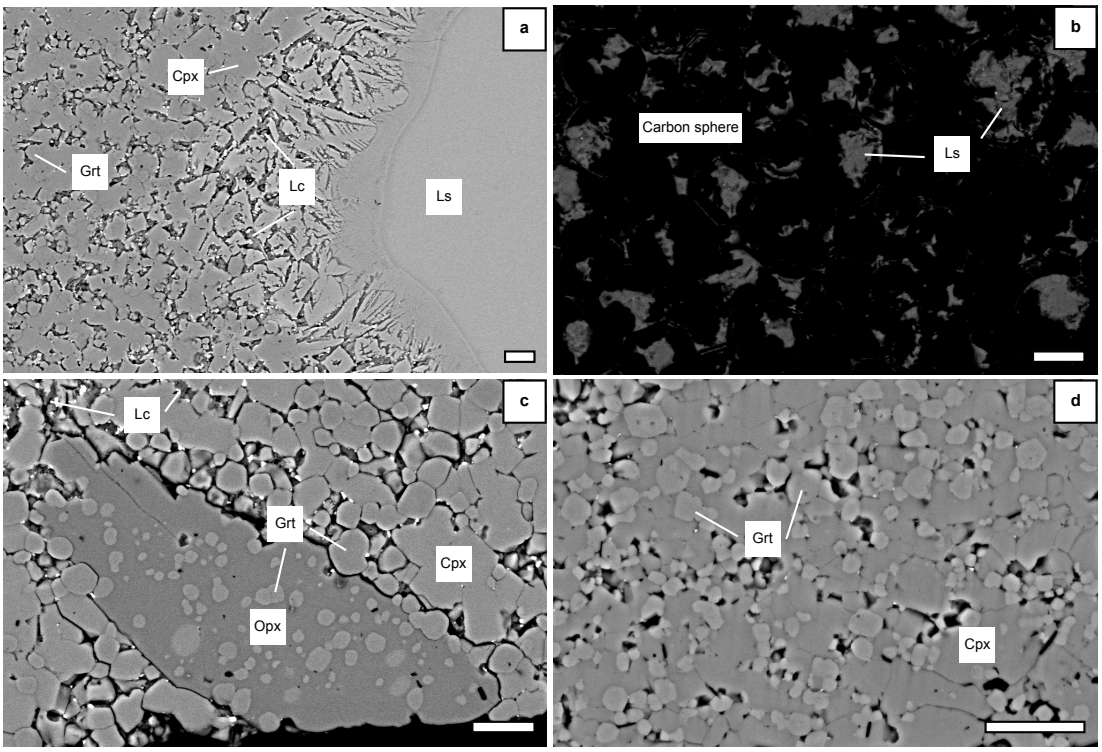

Supplementary Fig. 2. Backscattered electron images of run products from high-pressure crystallization experiments. Scale bars denote 20 μm. Ls, carbonated silicate melt; Lc, carbonate-rich melt; Cpx, clinopyroxene; Grt, garnet; Opx, orthopyroxene. **a**, MA19 at 1350 °C, containing a Ls pool and Lc in grain boundaries; **b**, MA18 at 1250 °C, with Ls trapped in carbon spheres; **c**, MA20 at 1200 °C, with a small amount of Opx. **d**, MA21 at 1150 °C, containing no Lc.

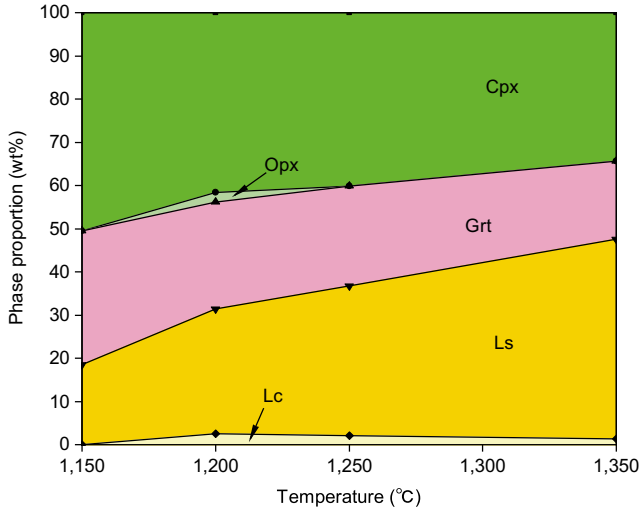

Supplementary Fig. 3. Calculated phase proportions of run products from high-pressure crystallization experiments at different temperatures. The experiments were performed at 3.0 GPa using CP-2 composition as the starting material. Results from the 1300 °C run (Run # MA16) are not listed here as disequilibrium behavior was observed in the sample charge (Methods). Mineral abbreviations are the same as in Supplementary Fig. 2.

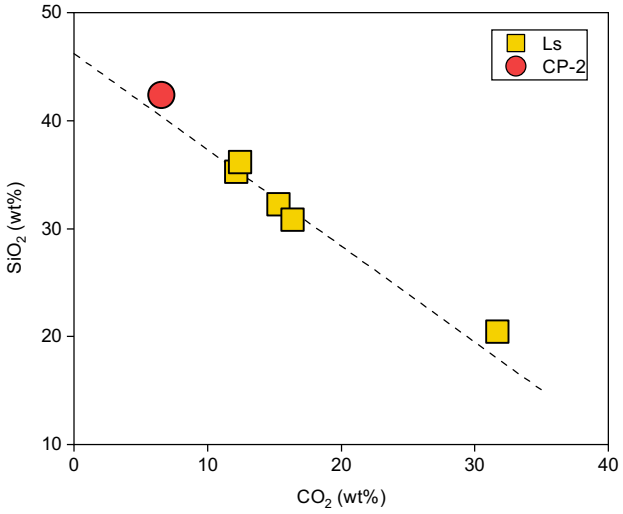

Supplementary Fig. 4. Measured SiO_2 contents plotted against the estimated CO_2 contents in Ls of run products from high-pressure crystallization experiments. The dashed line shows the linear fit line obtained by ref. [2]. All Ls compositions from our experiments fall on this line. It should be noted that the SiO_2 contents shown here are not normalized on a volatile-free basis, whereas melt SiO_2 contents reported in Figs. 1-3 and Supplementary Fig. 5 are normalized to volatile-free compositions.

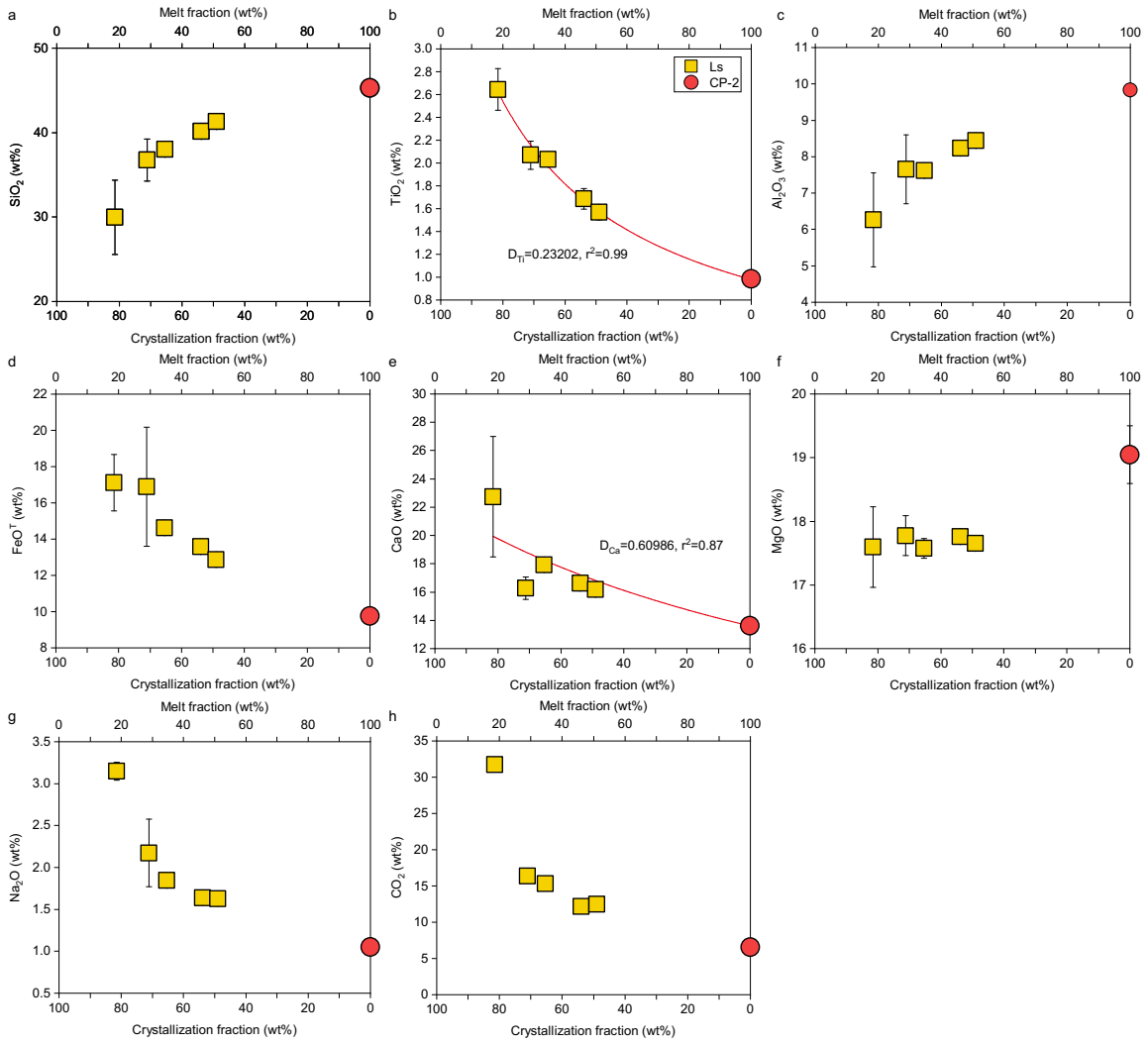

Supplementary Fig. 5. Geochemical variations of Ls in run products of high-pressure crystallization experiments as a function of crystallization fraction. The experiments were performed at 3.0 GPa using CP-2 composition as the starting material. All the major element oxide contents of Ls are recalculated to totals of 100%. The error bars represent one standard deviations. D_{Ti} and D_{Ca} are determined by fitting the experimental data (red line) using the equation (S1).

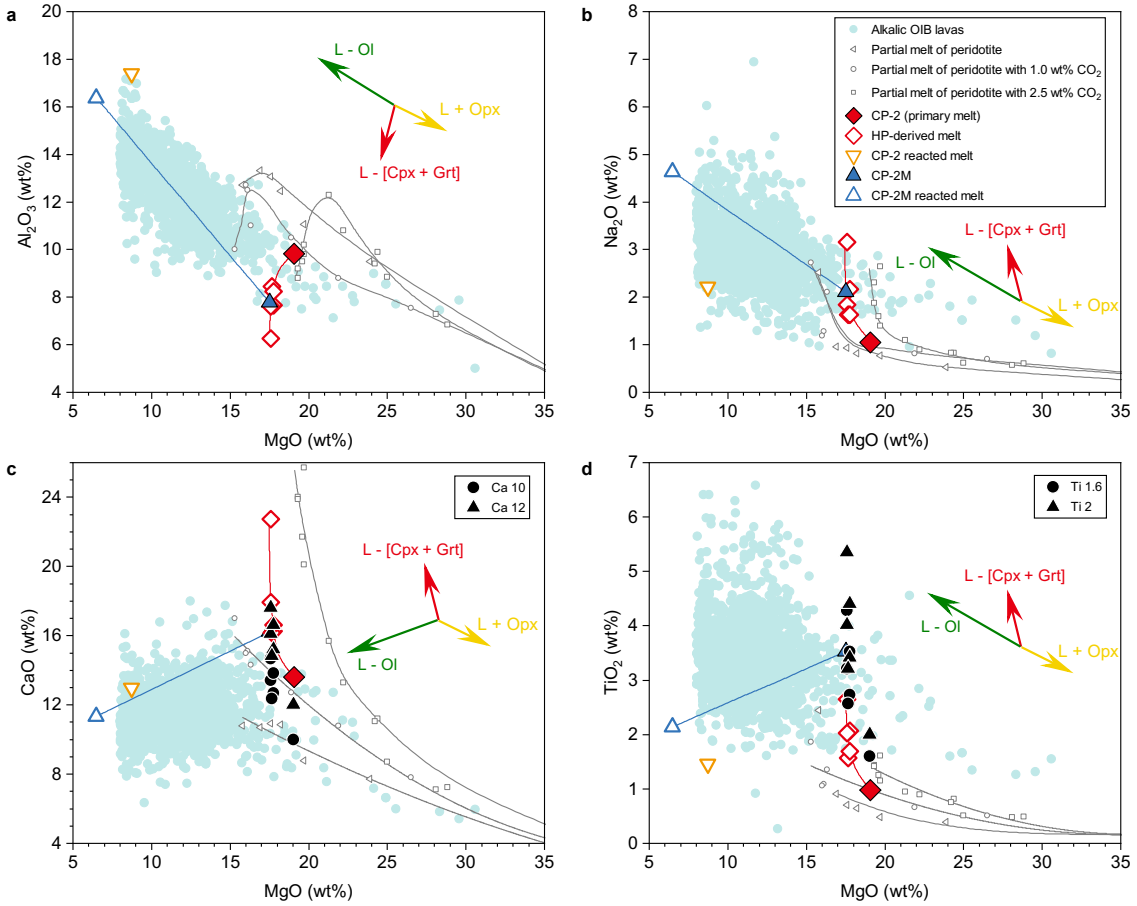

Supplementary Fig. 6. Evolution of Al_2O_3, Na_2O, CaO, and TiO_2 contents in carbonated alkalic OIB magmas. Symbols are the same as in Fig. 2. The numbers following Ca and Ti in the legends of **c** and **d** represent the starting CaO and TiO_2 contents in wt% in the primary magma. For example, Ti 1.6 indicates that the primary magma contains 1.6 wt% TiO_2. Arrows indicate the evolving directions of HP crystallization of clinopyroxene and garnet (Cpx and Grt, red), orthopyroxene (Opx) assimilation (yellow), and olivine (Ol) fractionation (green).

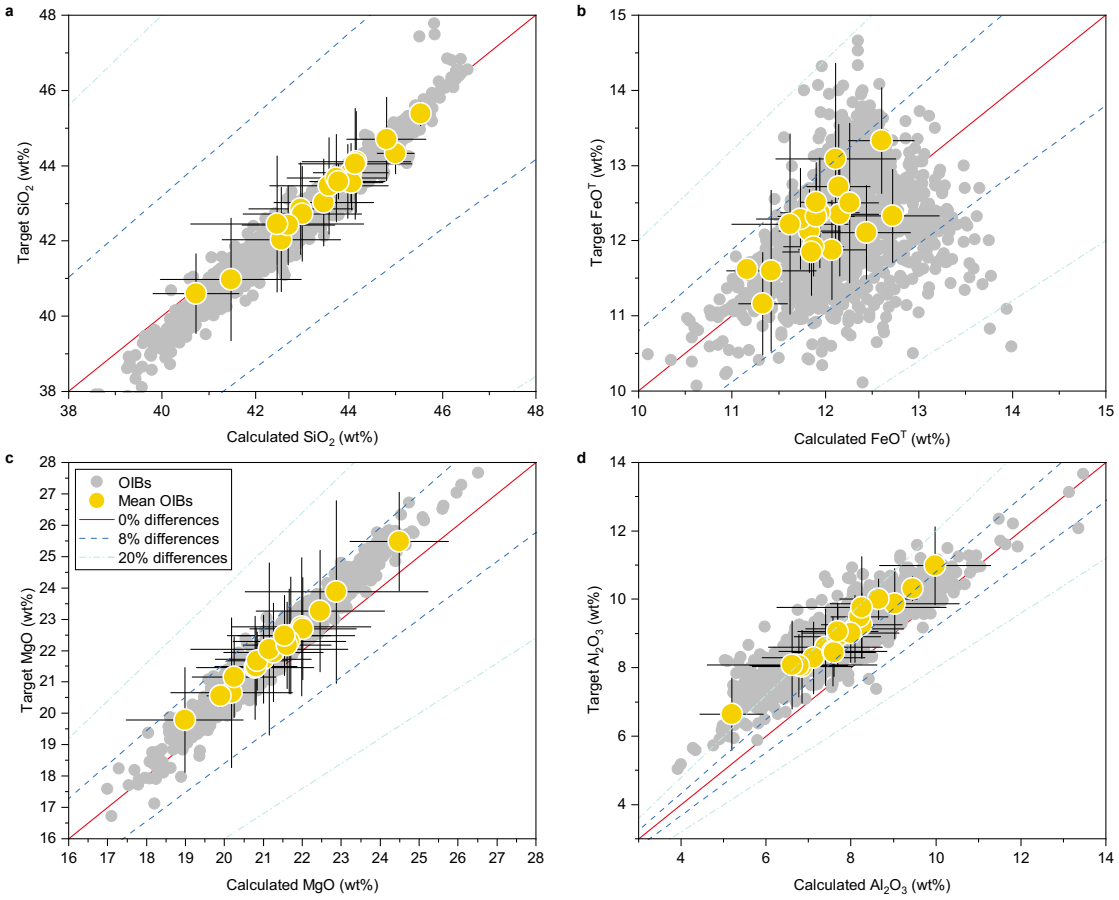

Supplementary Fig. 7. Comparison of calculated oxide contents with target oxide contents in parental OIBs. Gray circles represent all samples from individual ocean island. Yellow circles represent the mean values of individual ocean islands with error bars representing one standard deviations. Most mean values of calculated contents are within 8% differences of the target ones for SiO_2, MgO, and FeO^T, and within 20% differences for Al_2O_3.

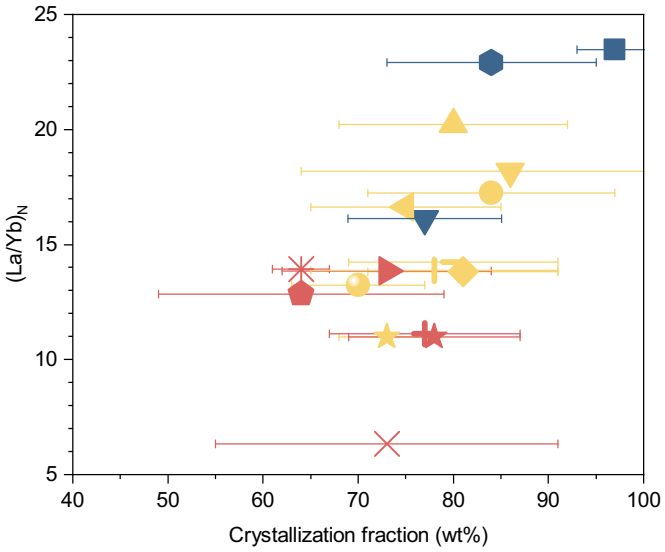

Supplementary Fig. 8. $(La/Yb)_N$ ratio plotted against crystallization fraction. The positive correlation suggests stronger garnet precipitation effects at higher degrees of crystallization fraction (CF). The La and Yb concentrations of samples in each ocean island are from GEOROC database and are normalized to the primitive mantle[11]. CF was calculated and averaged for individual island groups[12], with error bars representing one standard deviations. Symbols are the same as in Fig. 1.

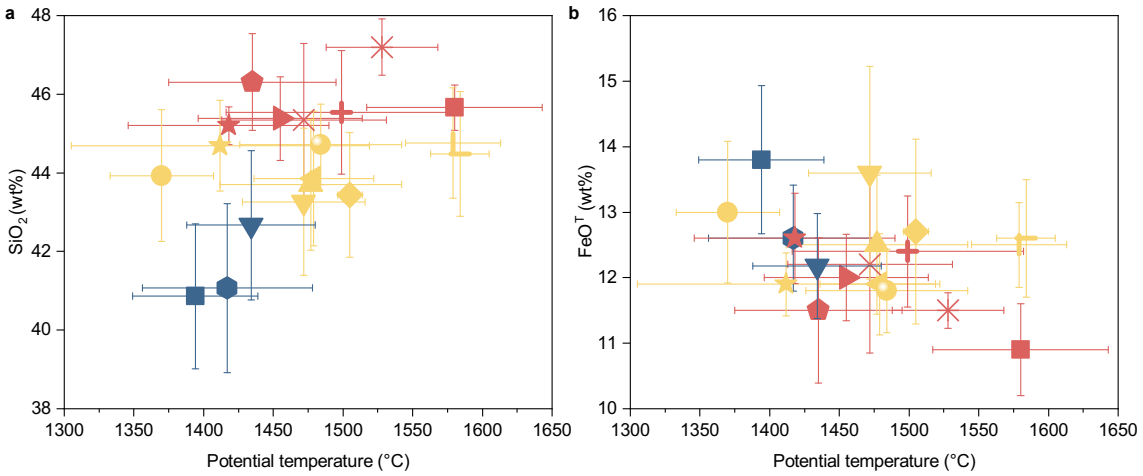

Supplementary Fig. 9. Intraplate OIB compositions plotted against mantle potential temperature (T_p). a, SiO_2-T_p plot. **b**, FeO^T-T_p plot. The SiO_2 and FeO^T contents of OIBs[12] show positive and negative correlation with T_p, respectively. Symbols are the same as in Fig. 1.

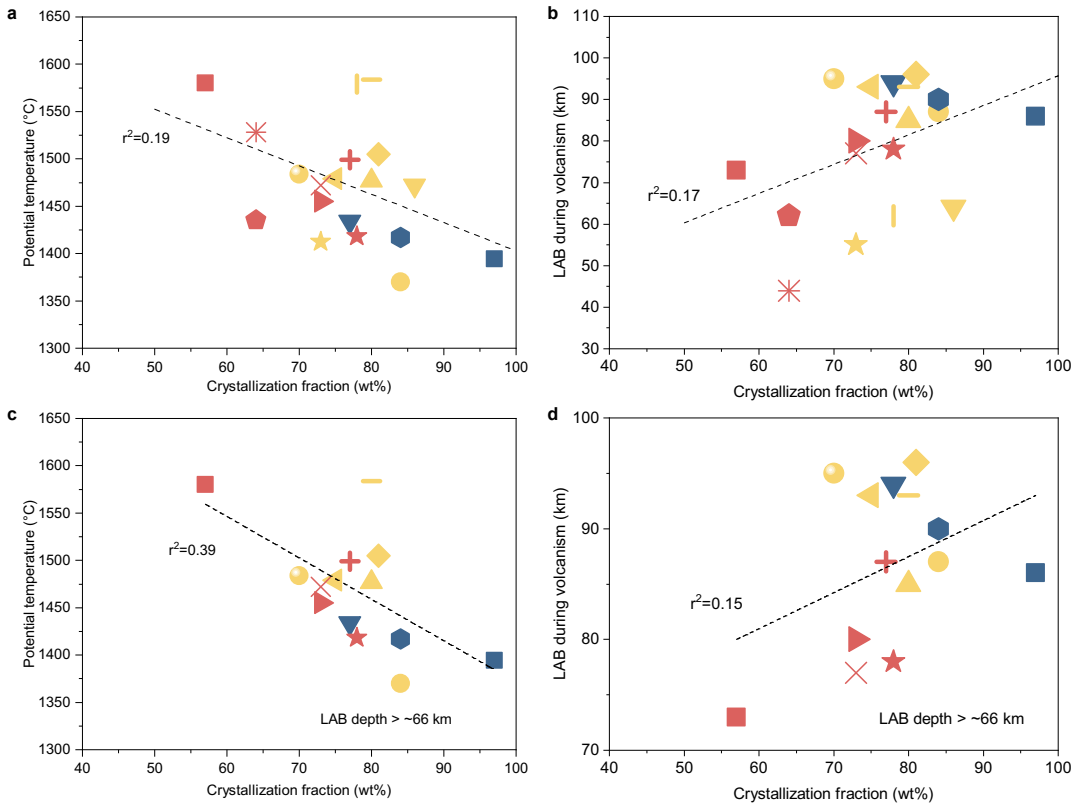

Supplementary Fig. 10. Intraplate OIB potential temperature (T_p) and lithospheric thickness plotted against high-pressure crystallization fraction. Mantle potential temperature is estimated by ref. [13] using seismic velocity observations, while lithospheric thickness corresponds to the lithosphere-asthenosphere boundary (LAB) depth during ocean island volcanism[1]. **a** and **b** include all alkalic OIBs. **c** and **d** are alkalic OIBs with LAB depth greater than ~66 km. Dash lines represent linear fitting and the symbols are the same as in Fig. 1.

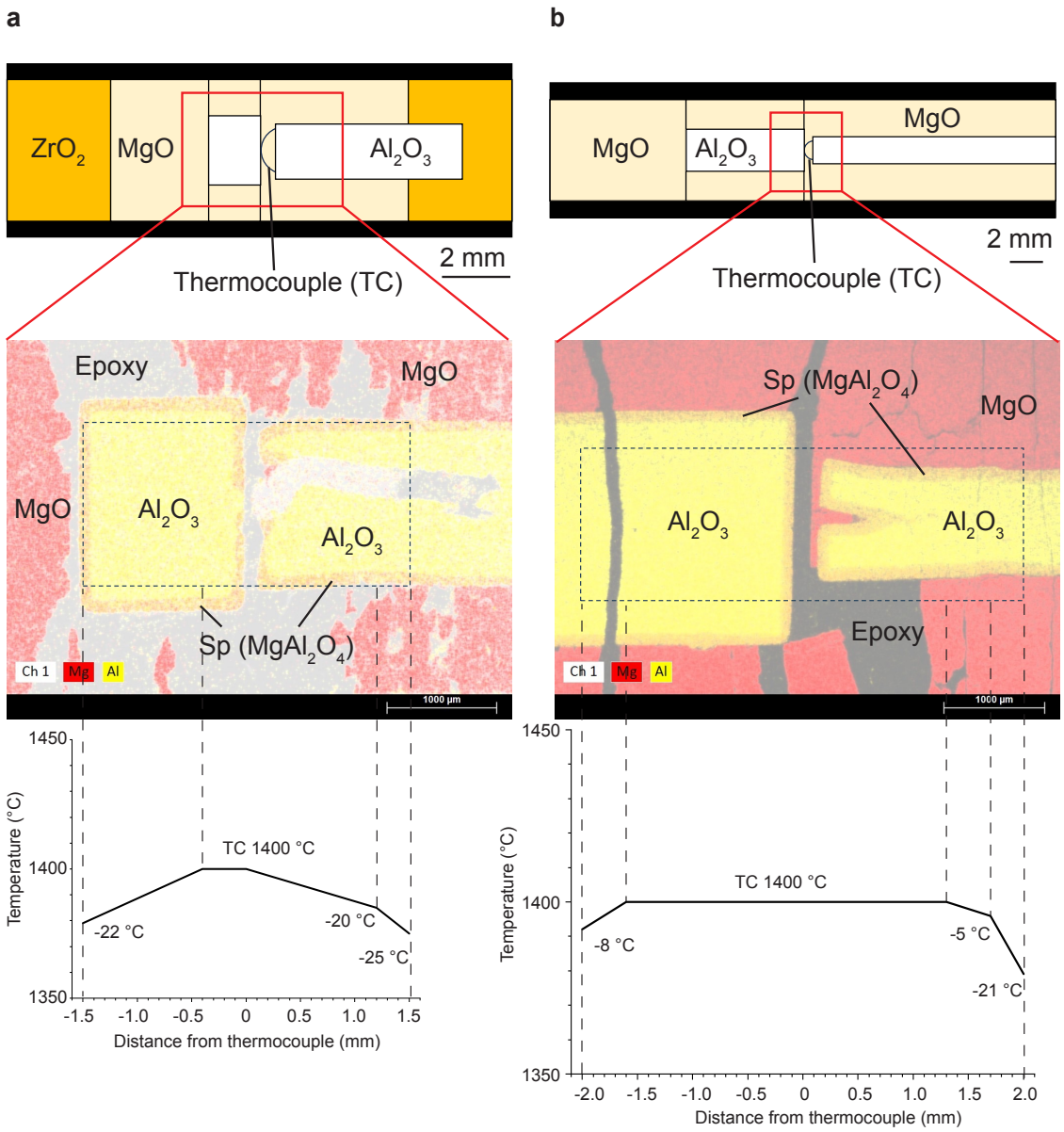

Supplementary Fig. 11. Schematic cross sections and backscattered electron mapping images for thermal calibration experiments. a, Calibration of thermal gradient in the multi-anvil cell assembly. **b**, Calibration of thermal gradient in the piston-cylinder assembly. The top panels show the respected cross sections of the cell assemblies. The central panels show the elemental mappings from BSE for the corresponding sample areas. The dashed boxes represent the sample capsule locations in the experiments. The bottom

panels show the calculated temperature profiles for samples in the multi-anvil and piston-cylinder presses based on measurements of spinel layer thickness[10].

Supplementary Table 1. Experimental conditions and compositions of run products for high-pressure crystallization experiments using CP-2 as starting material

Phase	N*	SiO_2	TiO_2	Al_2O_3	FeO^T	MnO	MgO	CaO	Na_2O	K_2O	Cr_2O_3	Total	Mg#	CO_2 (by diff.)†	Mode‡
Starting material															
CP-2	10	45.3(6)	0.98(4)	9.8(2)	9.8(2)	0.17(2)	19.1(5)	13.6(2)	1.05(3)	0.05(1)	0.21(2)	100.00	0.78	6.6(6)	100
MA19, 3GPa, 1350°C, 24h, R2§=0.37															
Grt	4	41.9(4)	0.6(2)	22.2(2)	9.0(1)	0.26(3)	19.6(3)	5.9(3)	0.03(2)	-	0.48(6)	99.83	0.80		18.1
Cpx	4	53.2(9)	0.20(5)	5.2(4)	6.4(1)	0.14(2)	20.5(2)	13.5(4)	0.69(4)	0.01(0)	0.23(3)	100.04	0.85		34.4
Lc	5	0.1(1)	0.04(3)	0.2(1)	8.3(5)	0.27(3)	12(2)	36.8(3)	0.06(2)	-	0.02(2)	57.81	0.72	42.2(15)	1.4
Ls	7	40.1(2)	1.69(9)	8.2(1)	13.6(1)	0.20(2)	17.8(1)	16.6(1)	1.63(3)	0.10(1)	0.06(2)	100.00	0.70	12.2(3)	46.1
MA16, 3GPa, 1300°C, 8h, R2=0.05															
Grt	5	42.1(2)	0.5(2)	22.2(2)	8.3(2)	0.22(4)	20.0(3)	5.9(3)	0.02(2)	-	0.6(1)	99.82	0.81		18.0
Cpx	5	53.8(3)	0.18(4)	4.5(2)	5.6(1)	0.11(3)	20.7(2)	13.8(2)	0.74(2)	0.01(1)	0.24(1)	99.79	0.87		30.6
Lc	6	0.2(2)	0.03(2)	0.1(1)	8.9(9)	0.31(5)	14(1)	35.8(8)	0.06(1)	0.01(1)	0.01(1)	59.64	0.74	40.4(15)	0.4
Ls	5	41.3(1)	1.57(6)	8.4(1)	12.9(2)	0.21(3)	17.7(1)	16.2(1)	1.63(7)	0.10(1)	0.07(1)	100.00	0.71	12.5(5)	51.0
MA18, 3GPa, 1250°C, 24h, R2=0.34															
Grt	5	41.8(5)	0.7(2)	22.2(4)	9.8(2)	0.24(2)	18.8(5)	6.1(5)	0.03(3)	0.01(1)	0.50(5)	100.21	0.77		23.1
Cpx	5	53.3(6)	0.28(5)	4.6(1)	6.7(3)	0.13(3)	20.0(4)	14.2(5)	0.73(5)	-	0.20(2)	100.13	0.84		40.2
Lc	4	0.3(3)	0.03(2)	0.2(1)	8(2)	0.32(9)	12.3(8)	33(2)	0.11(3)	-	0.01(1)	54.26	0.74	45.8(28)	2.1
Ls	8	38.0(1)	2.03(6)	7.6(1)	14.6(1)	0.20(2)	17.6(2)	17.9(2)	1.84(6)	0.14(1)	0.04(2)	100.00	0.68	15.3(8)	34.6
MA20, 3GPa, 1200°C, 48h, R2=0.90															
Grt	3	42.1(3)	0.5(3)	22.5(6)	9.6(4)	0.21(4)	19.1(7)	5.8(4)	0.02(2)	-	0.53(8)	100.27	0.78		24.7
Cpx	3	53.5(3)	0.23(3)	4.4(3)	6.0(3)	0.15(2)	19.5(4)	15.8(5)	0.73(5)	-	0.24(2)	100.58	0.85		41.7
Opx	3	54.2(3)	0.13(2)	4.5(1)	8.9(1)	0.16(2)	29.4(2)	2.1(1)	0.14(2)	-	0.21(4)				2.2
Lc	7	0.04(3)	0.04(3)	0.04(2)	7(1)	0.35(4)	15.0(9)	36(2)	0.06(3)	0.01(1)	0.03(1)	59.40	0.78	40.6(33)	2.5
Ls	5	37(3)	2.1(1)	8(1)	17(3)	0.24(7)	17.8(3)	16.3(8)	2.2(4)	0.15(4)	0.04(2)	100.00	0.65	16.4(52)	28.9
MA21, 3GPa, 1150°C, 48h, R2=4.9															
Grt	4	41.4(4)	0.91(7)	21.6(2)	12.2(2)	0.29(2)	17.0(2)	6.7(1)	0.05(3)	-	0.38(4)	100.56	0.71		31.0
Cpx	4	52.9(5)	0.73(7)	4.8(8)	6.5(4)	0.10(3)	17.2(7)	17.0(9)	1.02(4)	-	0.20(5)	100.50	0.82		50.5
Ls	4	30(4)	2.7(2)	6(1)	17(2)	0.26(3)	17.6(6)	23(4)	3.2(1)	0.27(3)	0.02(2)	100.00	0.65	31.7(106)	18.5

*N is the number of electron probe analyses used to obtain the average compositions.

†CO_2 (by diff.) is the estimated CO_2 content by subtracting electron microprobe totals for all other oxide components from 100 wt%.

‡Mode is the phase proportions (in wt%) calculated by mass balance.

§R2 is the sum of squared residuals in mass balance calculations.

Mg# is the mole ratio calculated as Mg/(Mg + Fe) and the total Fe is given as FeO (FeO^T). The values in parentheses are one standard deviation with respect to mean based on multiple electron microprobe analyses. For example, 45.3 (6) indicates 45.3 ± 0.6 wt%.

Supplementary Table 2. Experimental conditions and compositions (wt%) of run products for melt-orthopyroxene reaction experiments

Phase	N	SiO_2	TiO_2	Al_2O_3	FeO^T	MnO	MgO	CaO	Na_2O	K_2O	Cr_2O_3	Total	Mg#	CO_2 (by diff.)
Starting material														
CP-2M	5	36.4(1)	3.5(1)	7.8(1)	16.1(1)	0.27(4)	17.5(2)	16.2(4)	2.1(1)	0.10(5)	0.01(1)	100.00	0.66	10.1(7)
Opx	-	55.17	0.09	3.29	5.82	0.15	34.18	0.37	0.03	-	0.26	100.21	0.91	-
P25, 1.0GPa, 1200°C, 24h, Ol + Cpx + melt														
CP-2M reacted melt	4	50.2(11)	2.1(5)	16.4(5)	8.3(9)	0.18(4)	6.5(3)	11.3(8)	4.6(4)	0.31(4)	0.03(1)	100.00	0.58	1.7(7)
P24, 1.0GPa, 1200°C, 24h, Ol + Cpx + melt														
CP-2 reacted melt	3	47.7(4)	1.5(1)	17.4(6)	9.2(1)	0.19(2)	8.8(9)	13.0(4)	2.2(2)	0.15(5)	0.03(2)	100.00	0.63	2.3(1)

The values in parentheses are one standard deviation with respect to mean based on multiple electron microprobe analyses.

Supplementary Table 3. Estimated alkalic OIB mean compositions for each individual island groups

Location	N*	SiO_2	TiO_2	Al_2O_3	FeO^T	MnO	MgO	CaO	Na_2O	K_2O	P_2O_5	Total	SiO_2/FeO^T
Balleny	4	45.7(6)	2.6(1)	14.8(15)	10.9(7)	0.21(3)	10.3(13)	10.2(11)	3.7(6)	1.2(2)	0.6(1)	100	4.19
Cameroon	46	44.0(18)	3.2(9)	11.9(15)	13.0(11)	0.18(9)	11.9(29)	10.8(14)	3.0(6)	1.3(4)	0.9(3)	100	3.38
Canary	580	43.7(17)	3.4(7)	12.5(14)	12.5(11)	0.19(2)	11.3(23)	11.3(11)	3.2(6)	1.2(4)	0.8(2)	100	3.50
Cape Verde	506	42.7(19)	3.7(6)	12.3(13)	12.2(8)	0.19(2)	12.0(24)	12.5(13)	2.7(7)	1.1(5)	0.7(2)	100	3.50
Caroline	21	43.4(16)	3.6(6)	12.2(15)	12.7(14)	0.19(3)	11.2(23)	11.9(12)	3.0(8)	1.2(4)	0.7(3)	100	3.42
Comoros	75	43.9(17)	2.3(6)	12.1(12)	11.9(8)	0.20(2)	13.0(28)	11.8(10)	3.1(7)	1.1(3)	0.6(2)	100	3.69
Crozet	10	45.4(11)	3.0(4)	13.5(18)	12.0(7)	0.18(1)	9.9(24)	11.8(14)	2.7(5)	1.2(3)	0.5(2)	100	3.78
Fernando de Noronha	40	41.1(22)	3.4(6)	11.1(13)	12.6(8)	0.24(14)	13.3(17)	12.7(11)	3.3(6)	1.4(5)	0.9(2)	100	3.26
Juan Fernandez	18	44.7(12)	2.8(2)	13.0(10)	11.9(5)	0.19(5)	12.0(23)	9.8(9)	3.6(7)	1.4(5)	0.6(2)	100	3.76
Kerguelen	15	46.3(12)	3.1(4)	13.7(13)	11.5(11)	0.18(2)	10.5(15)	9.4(11)	3.2(6)	1.6(6)	0.7(2)	100	4.03
Madeira	109	44.8(11)	2.8(4)	13.9(10)	11.8(7)	0.20(3)	11.1(20)	11.0(7)	3.0(5)	0.9(2)	0.6(2)	100	3.79
Marquesas	46	45.7(18)	3.5(4)	13.0(13)	12.3(9)	0.19(5)	10.8(21)	9.9(13)	2.7(4)	1.4(4)	0.5(1)	100	3.67
Mascarene-Reunion	36	45.3(20)	2.3(6)	13.0(26)	12.2(14)	0.17(3)	13.6(62)	9.6(18)	2.8(6)	0.8(4)	0.3(2)	100	3.72
Pitcairn-Gambier	4	47.2(7)	3.0(6)	14.1(7)	11.5(3)	0.17(1)	10.7(19)	8.8(10)	3.1(2)	1.2(3)	0.4(3)	100	4.10
Samoan	91	44.6(17)	3.8(8)	11.9(9)	12.6(10)	0.17(1)	12.1(17)	10.2(10)	2.8(6)	1.4(4)	0.5(2)	100	3.53
Society	68	44.9(15)	3.3(4)	11.6(13)	12.5(7)	0.13(7)	12.7(28)	10.4(10)	2.7(4)	1.4(4)	0.5(1)	100	3.58
St Helena	5	45.2(5)	3.1(3)	13.7(8)	12.6(7)	0.19(2)	10.0(9)	11.3(4)	2.7(3)	0.99(4)	0.46(1)	100	3.59
Trindade-Vitoria	22	40.9(18)	4.5(11)	11.1(15)	13.8(11)	0.20(2)	10.9(16)	11.9(9)	4.1(9)	1.6(10)	0.9(2)	100	2.96
Tristan da Cunha	16	43.6(23)	3.7(6)	13.2(12)	13.4(18)	0.16(2)	9.3(13)	11.9(11)	2.7(5)	1.6(4)	0.5(2)	100	3.18

*N is the number of alkalic OIB data[12] used to obtain the mean compositions.

The values in parentheses are one standard deviation with respect to mean compositions (wt%).

Supplementary Table 4. The composition (wt%) of peridotite and its mixtures with 5 wt% subducted materials

	SiO_2	TiO_2	Al_2O_3	FeO^T	MnO	MgO	CaO	Total	Mg#
Peridotite*	44.90	0.16	4.26	8.02	0.13	37.30	3.45	98.22	0.89
Peridotite + 5 wt% GLOSS†	45.81	0.19	4.74	7.93	0.15	35.59	3.62	98.03	0.89
Peridotite + 5 wt% MORB‡	45.17	0.23	4.87	8.11	0.13	35.83	3.76	98.10	0.89
Peridotite + 5 wt% AOC§	45.64	0.29	5.03	7.80	0.13	35.57	3.35	97.81	0.89

*Peridotite composition is from ref. [14].

†GLOSS composition is from ref. [6].

‡MORB composition is from ref. [7].

§AOC composition is from ref. [8].

Alkali components (Na_2O and K_2O) are not listed here because they would likely dissolve into aqueous fluids or hydrous melts released during the dehydration of subducting slabs and be transported to the mantle wedge, limiting their influence on the source peridotite for OIBs.

Supplementary Table 5. Estimated potential temperature, high-pressure crystallization fraction, melt-orthopyroxene reaction fraction, and carbon contents and flux at individual ocean island locations

Location	T_p*	N†	CF (%)	RF (%)	CO_2 (wt%) in primary magma	CO_2 (wt%) in evolved magma (CF+RF)	C-flux (Mt/yr)
Balleny	1580(63)	4	57(10)	17(9)	2.3(5)	3(1)	41(13)
Cameroon	1370(37)	46	84(13)	37(10)	3.9(12)	7(2)	106(30)
Canary	1477(65)	580	80(12)	33(9)	3.5(8)	7(3)	103(38)
Cape Verde	1434(46)	506	78(8)	28(7)	3.5(5)	8(2)	117(37)
Caroline	1505(9)	21	81(10)	34(10)	3.7(8)	8(2)	112(29)
Comoros	1479(43)	75	75(10)	28(9)	3.1(7)	6(2)	89(32)
Crozet	1455(59)	10	73(11)	28(7)	2.9(5)	5(2)	71(25)
Fernando de Noronha	1417(61)	40	84(11)	33(8)	4.1(6)	10(3)	147(44)
Juan Fernandez	1412(107)	18	73(5)	28(4)	2.9(5)	5(2)	73(25)
Kerguelen	1435(60)	15	64(15)	24(11)	2.6(11)	3(2)	47(28)
Madeira	1484(58)	109	70(7)	25(6)	2.9(4)	5(1)	72(21)
Marquesas	1499(83)	46	77(10)	31(7)	2.9(10)	5(2)	70(34)
Mascarene-Reunion	1472(59)	36	73(18)	30(12)	2.7(11)	5(3)	68(38)
Pitcairn-Gambier	1528(40)	4	64(3)	24(3)	1.9(2)	1.5(4)	23(6)
Samoan	1584(21)	91	80(11)	34(8)	3.2(9)	6(2)	88(36)
Society	1579(34)	68	78(13)	33(8)	3.3(7)	6(2)	83(31)
St Helena	1418(72)	5	78(9)	32(7)	3.1(3)	5(1)	80(19)
Trindade-Vitoria	1394(45)	22	97(4)	47(6)	4.9(9)	11(2)	169(26)
Tristan da Cunha	1472(44)	16	86(22)	39(15)	4.2(8)	8(3)	126(49)

*T_p is mantle potential temperature estimated by geophysical observations from ref. [13].

†N is the number of alkalic OIB data[12] used to obtain the mean values.

The estimated evolved CO_2 contents ($X_{CO_2}^{Evol}$) of each individual ocean island are based on the correlation between $X_{SiO_2}^{Calc}$ and $X_{CO_2}^{Evol}$ in Supplementary Fig. 4. For data with $X_{SiO_2}^{Calc} >$ 46 wt% (in total 13 data points), the calculated $X_{CO_2}^{Evol}$ is less than 0. Thus we set $X_{CO_2}^{Evol} =$ 0 for these data points.

The values in parentheses are one standard deviation with respect to mean values.

Supplementary Table 6. The starting bulk compositions (wt%) for partial melting experiments of carbon-free peridotite and carbonated peridotite, and HP-crystallization of the carbon-free picritic melt in Fig. 3 of the main text

Component	No.	SiO_2	TiO_2	Al_2O_3	FeO^T	MnO	MgO	CaO	Na_2O	K_2O	Cr_2O_3	Total	Mg#
Carbon-free peridotite	KR4003*	44.90	0.16	4.26	8.02	0.13	37.30	3.45	0.22	0.09	0.41	98.94	0.89
Carbonated peridotite	PERC3†	43.63	0.20	3.63	8.08	0.14	39.27	3.52	0.30	0.01	0.22	99.00	0.90
Carbon-free picritic melt	P19‡	46.50	0.80	13.13	9.09	0.10	18.50	10.33	0.81	0.48	0.19	99.93	0.78

*Bulk carbon-free peridotite composition is from ref. [14].

†Bulk carbonated peridotite composition is from ref. [2].

‡ Bulk carbon-free picritic melt composition is from ref. [15].

Supplementary Table 7. Fitted model parameters for the effects of high-pressure crystallization and melt-orthopyroxene reaction

Element i	SiO_2	MgO	FeO^T	Al_2O_3
a_i	42.09343	12.57138	14.81859	11.59123
b_i	-3.19293	0.67943	0.87966	-1.03355
c_i	0.07156	0.05349	-0.09108	0.04187
d_i	0.08079	-0.00522	-0.01437	0.00936
e_i	-2.9050×10^{-4}	0	3.4523×10^{-4}	-2.2427×10^{-4}
f_i	-5.0532×10^{-4}	0	6.4405×10^{-5}	-4.6064×10^{-5}

The parameters are used in Eqs. (2-4).

References

1 Dasgupta, R., Jackson, M. G. & Lee, C.-T. A. Major element chemistry of ocean island basalts — Conditions of mantle melting and heterogeneity of mantle source. *Earth Planet. Sci. Lett.* **289**, 377-392 (2010).

2 Dasgupta, R., Hirschmann, M. M. & Smith, N. D. Partial melting experiments of peridotite + CO_2 at 3 GPa and genesis of alkalic ocean island basalts. *J. Petrol.* **48**, 2093-2124 (2007).

3 Herzberg, C. Petrology and thermal structure of the Hawaiian plume from Mauna Kea volcano. *Nature* **444**, 605-609 (2006).

4 Dasgupta, R., Chi, H., Shimizu, N., Buono, A. S. & Walker, D. Carbon solution and partitioning between metallic and silicate melts in a shallow magma ocean: implications for the origin and distribution of terrestrial carbon. *Geochim. Cosmochim. Acta* **102**, 191-212 (2013).

5 Prytulak, J. & Elliott, T. TiO_2 enrichment in ocean island basalts. *Earth Planet. Sci. Lett.* **263**, 388-403 (2007).

6 Plank, T. in *Treatise on Geochemistry (Second Edition)* (eds Heinrich D. Holland & Karl K. Turekian) 607-629 (Elsevier, 2014).

7 Yaxley, G. & Green, D. Reactions between eclogite and peridotite: Mantle refertilisation by subduction of oceanic crust. *Schweiz. Mineral. Petrogr. Mitt.* **78**, 243-255 (1998).

8 Kelley, K. A., Plank, T., Ludden, J. & Staudigel, H. Composition of altered oceanic crust at ODP Sites 801 and 1149. *Geochem. Geophys. Geosyst.* **4** (2003).

9 Niu, Y. & O'Hara, M. J. Origin of ocean island basalts: A new perspective from

petrology, geochemistry, and mineral physics considerations. *J. Geophys. Res.* **108**, 2209 (2003).

10 Watson, E., Wark, D., Price, J. & Van Orman, J. Mapping the thermal structure of solid-media pressure assemblies. *Contrib. Mineral. Petrol.* **142**, 640-652 (2002).

11 Hofmann, A. W. Chemical differentiation of the Earth: the relationship between mantle, continental crust, and oceanic crust. *Earth Planet. Sci. Lett.* **90**, 297-314 (1988).

12 Sun, C. & Dasgupta, R. Carbon budget of Earth's deep mantle constrained by petrogenesis of silica-poor ocean island basalts. *Earth Planet. Sci. Lett.* **611**, 118135 (2023).

13 Bao, X., Lithgow-Bertelloni, C. R., Jackson, M. G. & Romanowicz, B. On the relative temperatures of Earth’s volcanic hotspots and mid-ocean ridges. *Science* **375**, 57-61 (2022).

14 Walter, M. J. Melting of garnet peridotite and the origin of komatiite and depleted lithosphere. *J. Petrol.* **39**, 29-60 (1998).

15 Yang, J., Wang, C., Zhang, J. & Jin, Z. Genesis of Hawaiian lavas by crystallization of picritic magma in the deep mantle. *Nat. Commun.* **14**, 1382 (2023).